Fifth International Symposium on Marine Propulsors
smp'17, Espoo, Finland, June 2017

RANS Simulations of Tip Leakage Vortex Cavitation Flows around NACA0009 Hydrofoil

Zhihui Liu[1], Benlong Wang[1,2*]

[1]MOE Key Laboratory of Hydrodynamics, Shanghai Jiao Tong University, 200240, Shanghai, China.
[2]Collaborative Innovation Center for Advanced Ship and Deep-Sea Exploration (CISSE), 200240, Shanghai, China.

ABSTRACT

Tip-leakage vortex cavitation can lead to thrust breakdown and blade vibration in hydraulic turbines. Numerical simulations of full wet and cavitating tip leakage vortex flows are studied. By comparing vortex structures, strain rates and Reynolds shear stresses distributions in the vortex region for full wet flows between numerical and experimental results of NACA0015 blade, it is found that the numerical results with the nonlinear k-ε turbulence model is in good agreement with the experimental results. Both full wet and cavitating flows around a NACA0009 blade with various gaps between the tip and end-wall are studied to investigate the influence of gap width on the development of tip vortex and tip vortex cavitation. Good agreements are obtained on the trajectories of tip leakage vortex by comparing the numerical results and experimental data. when the dimensionless gap size $\tau \leq 0.7$, numerical results show that there is an apparent difference on the vertex trajectories behind the hydrofoil between full wet and cavitating flows.

Keywords

Tip-leakage vortex, cavitation, turbulence model, OpenFOAM.

1 INTRODUCTION

Cavitation is a phenomenon that plays an important role in surface sea-going vessels, as well as in hydraulic equipments including hydrofoils, propellers, turbines and pumps. The tip-leakage vortex cavitation, which can lead to thrust breakdown and blade vibration, can be observed frequently in turbo-machine with a radial clearance between the rotor-blade tip and the casing wall. Complex vortex structures, including the induced vortex, tip-leakage vortex and tip-separation vortex, can be observed in the gap region (You et al., 2007). Due to the difficulties of numerical simulation of vortex flows (Salvatore et al., 2009; Sipilä et al., 2011; Vaz G, Hally D, Huuva T, et al, 2015), more advanced numerical models are desired to capture the main characteristic of the flow structures.

Using both LES and RANS, Decaix et al. (2015) simulated the wet flow around the NACA0009 hydrofoil, and proposed an empirical formulation for the vortex trajectory from the leading edge to the mid-chord.

Although DES and LES have been successfully applied in many cavitating flows, the Reynoldes-averaged Navier-Stokes (RANS) model remains the primary CFD solver used in practical applications for its low computational costs. Most of the RANS models are based on the Boussinesq turbulent-viscosity hypothesis, which has been used successfully in many turbulence flows dominated by shear stress. In this kind of flow, the orientations of the strain rate tensor and Reynolds stress tensor coincide. However, this type of linear model fails when the flow stream is strongly curved or rotated. Experimental observations show that the strain rate and Reynolds stress are not aligned in their tip vortex region Chow et al. (1997). Churchfield and Blaisdell (2009) explored several turbulence models and corrections for rotating flows with curvature streamlines, including one-equation model, two-equation models and shear stress transport model. It was found that none of these turbulence models can accurately capture the spatial lag between the Reynolds stress components and the corresponding strain rate components within the vortex. Thus, a nonlinear k-ε model is employed in the present study which has been successfully applied for tip vortex simulations in previous studies Liu2016. Numerical simulations for various gap size τ are conducted for both full wet and cavitating flows.

2 PROBLEM DISCRIPTIONS

2.1 Governing Flow Equations

To simulate the cavitating flows around hydrofoils and propellers, the assumption of a homogeneous mixed fluid of water and vapor is introduced. The liquid and vapor phases are assumed to be fully mixed and share the same velocity and pressure in the flow field. Therefore, only one set of RANS equations is used to model the flows. The continuity and momentum equations for the mixture are:

$$\frac{\partial \rho_m}{\partial t} + \frac{\partial \rho_m u_i}{\partial x_i} = 0 \tag{1}$$

$$\frac{\partial}{\partial t}(\rho_m u_i) + \frac{\partial}{\partial x_j}(\rho_m u_i u_j) = -\frac{\partial p}{\partial x_i} + \frac{\partial}{\partial x_j}\left[\mu_m\left(\frac{\partial u_i}{\partial x_j} + \frac{\partial u_j}{\partial x_i}\right)\right] + \frac{\partial \rho_m \tau_{ij}}{\partial x_j} \tag{2}$$

Where $\rho_m = \rho_l \alpha_l + \rho_v \alpha_v$ and $\mu_m = \mu_l \alpha_l + \mu_v \alpha_v$ are the average density and dynamic viscous coefficient; τ_{ij} is the

*Corresponding author: benlongwang@sjtu.edu.cn

Reynolds stress. The subscripts l and v denote liquid and vapor, respectively.

2.2 Numerical Methods

The numerical models are solved by using a flow solver OpenFOAM with finite volume method. The PISO scheme is used to solve the velocity/pressure coupling between the momentum and continuity equations. A second-order upwind scheme is used for the spatial discretization in the momentum equations and transport equations for k and ε. The QUICK scheme is used in the advection of the volume fraction function. The viscous terms are solved using a second-order central difference scheme.

2.3 Turbulence Model

In present work, turbulence models for RANS are investigated. The nonlinear $k-\varepsilon$ model proposed by Zhu and Shih (1994) is used, in which the turbulent shear stress can be expressed as:

$$\tau_{ij} = -\frac{2}{3}k\delta_{ij} + C_d\frac{k^2}{\varepsilon}S_{ij} + \frac{k^3}{(1000+\eta)\varepsilon^2}(-4T_{ij}^{(1)} + 13T_{ij}^{(2)} - 2T_{ij}^{(3)}) \tag{3}$$

where

$$T_{ij}^{(1)} = \frac{\partial u_i}{\partial x_l}\frac{\partial u_l}{\partial x_j} + \frac{\partial u_j}{\partial x_l}\frac{\partial u_l}{\partial x_i} - \frac{2}{3}\frac{\partial u_l}{\partial x_k}\frac{\partial u_k}{\partial x_l}\delta_{ij}$$

$$T_{ij}^{(2)} = \frac{\partial u_i}{\partial x_k}\frac{\partial u_j}{\partial x_k} - \frac{1}{3}\frac{\partial u_l}{\partial x_k}\frac{\partial u_l}{\partial x_k}\delta_{ij}$$

$$T_{ij}^{(3)} = \frac{\partial u_k}{\partial x_i}\frac{\partial u_k}{\partial x_j} - \frac{1}{3}\frac{\partial u_l}{\partial x_k}\frac{\partial u_l}{\partial x_k}\delta_{ij}$$

$$C_d = \frac{2}{3}\left(1.25 + \delta + 0.9\frac{k}{\epsilon}\Omega\right)^{-1}$$

and $\eta = Sk/\varepsilon$. In this turbulence model, the rotation rate Ω is also included in the constitute relationship. The rotational effect of the mean flow is described by C_d. The nonlinear k-ε model is a high-Reynolds-number model with wall functions, denoted as NonlinearKEShih in OpenFOAM, which is also known as the realizable Reynolds stress algebraic equation model. Although the theoretical foundation of the nonlinear $k-\varepsilon$ model is significantly different from that of the standard $k-\varepsilon$ model, the nonlinear $k-\varepsilon$ model using the same transport equations for the turbulent kinetic energy k and dissipation rate ε as the standard $k-\varepsilon$ model Launder and Spalding (1974).

2.4 Cavitation Model

To simulate the phase transition between the liquid and vapor phases, a cavitation model is needed. The transport equation model has been widely used in recent numerical studies of cavitating flows. Examples of such models are given by Schnerr and Sauer (2001), Singhal et al. (2002) and Zwart et al. (2004). These types of cavitation models have been successfully used in simulations of various unsteady cavitating flows. The transport equation of Schnerr and Sauer (2001) is used in the present work:

$$\frac{\partial \alpha_l\rho_l}{\partial t} + \frac{\partial \alpha_l\rho_l u_j}{\partial x_j} = \dot{m} = \frac{\rho_v\rho_l}{\rho_m}\alpha_v\alpha_l\frac{3}{R_B}\sqrt{\frac{2}{3}\frac{|P_v - P|}{\rho_l}}sign(P_v - P) \tag{4}$$

where

$$\alpha_v = 1 - \alpha_l, \quad R_B = \left(\frac{\alpha_v}{\alpha_l}\frac{3}{4\pi}\frac{1}{n}\right)^{\frac{1}{3}}$$

n is the number density of cavitation bubble, P_v is the saturated vapor pressure, $sign$ is the sign function.

2.5 Computational Domain and Boundary Conditions

Three type boundaries are used in the simulations: (1) inlet boundary condition, where the velocity is specified and values of VOF function are set to $\alpha_v = 0$; (2) outlet boundary condition, where the pressure is prescribed according to the cavitation number, the normal gradient of velocity and other scalar function are set to zero; (3) no slip boundary condition at the hydrofoil surface, where the velocity components are all set to zero at wall surface, and the normal gradient of the scalar function (e.g. pressure or VOF function) is set to zero. The boundary conditions for k and ε are specified at the inlet: $k = \frac{3}{2}(UI)^2$, $\varepsilon = C_\mu^{0.75}k^{1.5}/C$, which are also given as the initial conditions in the computational domain. U is the incoming velocity, I=0.05 is the turbulence intensity, and the character length takes the value of the chord length C.

3 VALIDATIONS OF NUMERICAL METHODS

In this work, simulations of tip vortex flows around a NACA0015 hydrofoil is used to verify the proposed numerical method, following the same setup as the experiments conducted by Chow et al. (1997). Two different kind of turbulence models are used to simulate the flow around a NACA0015 blade with no confinement on the tip side, i.e. the wall is fall away from the wing tip.

Multi-block structural meshes are used in this study to improve the mesh quality. In order to capture the vortex structures, the strategies of mesh refinement are also investigated. A full structural mesh with a C-type block is generated around the NACA0015 hydrofoil. In order to capture the complex cloud cavitation structure and the detail vortex structures, computational mesh is refined in the suction side than that in the pressure side. The grid in the near field behind the hydrofoil is also refined to capture the fine structures of cavitation and vortex. The computational domain and the mesh around the hydrofoil are shown in Figure 1. There are 3C (chord length) from the leading edge of the hydrofoil to the front side of the computational domain, 6C from the trailing edge of the hydrofoil to the end of the computational domain, and 4C from both top and bottom sides of the computational domain. The values of y^+ are around 30 at the surface of the hydrofoil to use the wall function. In this study the incoming velocity U = 2.02m/s, the angle of attack of twisted hydrofoil is $\alpha = 10^o$, the chord length is C = 0.1m. The total cell number is 1.2 million after the mesh refinement in the tip region.

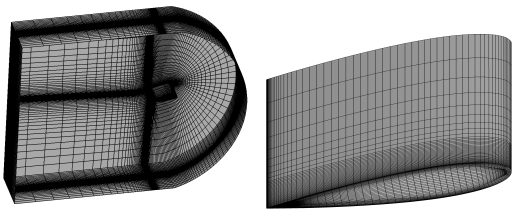

Figure 1: Mesh distribution in the computational domain and at the surface of the NACA0015 hydrofoil

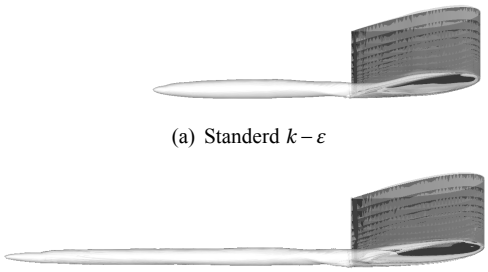

(a) Standerd $k-\varepsilon$

(b) Nonlinear $k-\varepsilon$

Figure 2: Iso-surface with $Q = 10^3$, at the same mesh resolution.

The definition of Q-criterion (Jeong and Hussain, 1995) :

$$Q = \frac{1}{4}\left(\frac{\partial v}{\partial y} + \frac{\partial w}{\partial z}\right)^2 + \frac{\partial v}{\partial z}\frac{\partial w}{\partial y} - \frac{\partial w}{\partial z}\frac{\partial v}{\partial y}$$

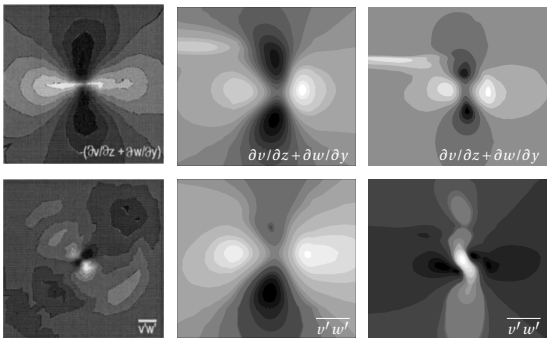

(a) Experimental results (b) Standerd $k-\varepsilon$ (c) Nonlinear $k-\varepsilon$

Figure 3: Comparison of spatial distribution of negative strain rate and deviatoric Reynolds stress between experiment results (Chow et al., 1997) and numerical simulations: $Re = 4.6 \times 10^6$, $x = 1.452C$.

At the same mesh resolution, the computational results for the two different turbulence models are shown in Figure 2. The range of the iso-surface of Q extends much more longer in the simulations with the nonlinear $k-\varepsilon$ turbulence model than that with the standard k-ε model.

The measurements of the tip vortex flow were conducted at various attach angles ($4^o - 12^o$) and Reynolds numbers ($5 \times 10^5 - 4.6 \times 10^6$) (Chow et al., 1997; Giuni, 2013). Four-lobe patterns were found for both the strain rate and the Reynolds stress in these experimental results. All experimental results show that there is a spatial phase shift of the four-lobe pattern between the strain rate and the Reynolds stress, as shown in Figure 3(a): a phase shift of $\pi/4$ can be observed between the strain rates $\partial v/\partial z + \partial w/\partial y$ and the corresponding components of the Reynolds stress $\overline{v'w'}$. The numerical results with the nonlinear k-ε model predicts the same flow pattern as that obtained in experiments, which indicates the advantages of the nonlinear turbulence model on simulating the vortex flows. Then the nonlinear turbulence model will be used in the following studies.

4 RESULTS AND DISCUSSIONS

To investigate the influence of the gap size on the tip leakage vortex, the flows around a truncated NACA0009 hydrofoil are simulated with the nonlinear $k-\varepsilon$ model. The setup follows the water tunnel experiments of Dreyer et al. (2014). The hydrofoil is mounted on a vertical plate with an angle of attack $\alpha = 10^o$. There is a gap between the free end and the vertical plate. The incoming velocity is 10m/s and the cavitation number is $\sigma = 1.94$. The chord length of the truncated hydrofoil is $C = 0.1$ m, the span width is 0.15 m, and its maximum thickness h is 9.9 mm. The length of the gap is ℓ. The normalized gap width is defined as $\tau = \ell/h$.

A H-type multi-block structural meshes is used. Mesh is refined in the suction side because the tip leakage vortex will drift upward. To capture the leakage tip vortex structures, the mesh is refined in the gap region as well. Three different kinds of mesh structures are shown in Figure 4 for different gap size τ. From the experimental results of Dreyer et al. (2014) we can see that, when $\tau = 2$ the tip vortex trajectory have no obvious float upward, so the vortex structures will concentrated in the cord line and the mesh nods should concentrate in this line too (see Figure 4(a)). For $\tau = 1.5$ and $\tau = 1$ the tip vortex trajectory have just a tiny drift upward behind the wing section, so the mesh for this two gaps should have the same structure (show in Figure 4(b)). When the non-dimensional gap from 0.7 to 0.1, more meshes are arranged in the suction side of the wing section (see Figure 4(c)) after preliminary simulations. In this study the incoming velocity is $U = 10m/s$, the Reynolds number based on the hydrofoil chord is $Re_c = UC/\nu = 1 \times 10^6$. After preliminary mesh convergence tests, there are 200 nodes along the span and the suction side, and 100 nodes on the pressure side along the chord direction. The averaged y^+ is set to be 60 around the hydrofoil when $\tau \geq 1$, and the total cell number is around 2 million. Node numbers are 30, 25 and 20 in the gap region for $\tau = 2$, 1.5 and 1.0 respectively. The averaged y^+ is set to be 40 around the hydrofoil when $\tau \leq 0.7$, and the total cell number is around 4 million. For cases with narrow gap of $\tau \leq 0.7$, the node number in the gap in the span direction are listed in Table 1.

Table 1: node number in the gap in the span direction

τ	0.7	0.5	0.4	0.3	0.2	0.1
node number	28	25	23	20	18	12

Two gaps large than $\tau = 1$ and six gaps no wider than $\tau = 0.7$ are studied in this paper, for brevity, only five of these cases are compared with the experiments. Instantaneous snap shots of cavitation region are compare with high-speed camera pictures, as shown in Figure 5-9. Main cavitation

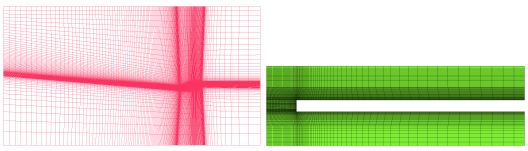

(a) $\tau = 2.0$

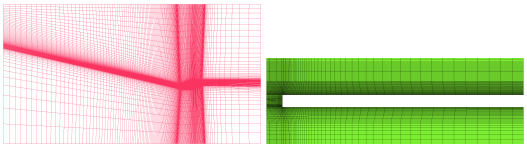

(b) $\tau = 1.0$

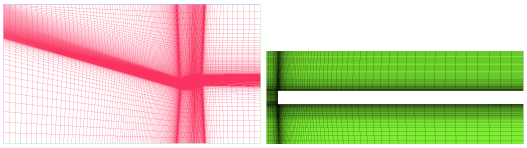

(c) $\tau = 0.7$

Figure 4: Mesh distribution of NACA0009, left: streamwise direction; right: transverse direction.

regions have been captured using the proposed numerical methods. When $\tau \geq 1.0$, two clear vortex tubes can be identified in the tip leakage vortex region from the contours of Q shown in the sub-figures (c) and (d). When the gap size further decreases, there is no clear cavitating vortex tube in the pressure side of the hydrofoil. The behavior of the cavitating flows at the tip section is more like a sheet cavitation, caused by the flow separation at the free end of the hydrofoil.

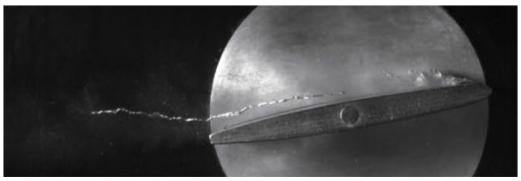

(a) experiment results from Dreyer et al. (2014)

(b) cavitation region marked by the isosurface of vapor valume fraction $\alpha = 0.5$

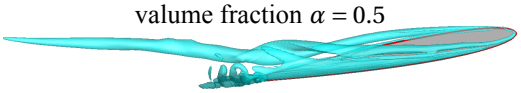

(c) isosurface of $Q = 1 \times 10^6$, full wet flow,

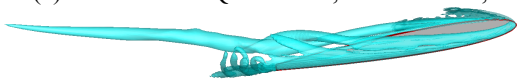

(d) isosurface of $Q = 1 \times 10^6$, cavitating flow

Figure 5: Comparisons on the vorticity region and cavitation region, $\tau = 2.0$.

In this stage a qualitative analysis between numerical and experimental results will be discussed. By comparing the Q isosurface show in Figure 5 with the experimental data obtained by Dreyer et al. (2014) , we find that the vortex structures with and without cavitation match the experimental

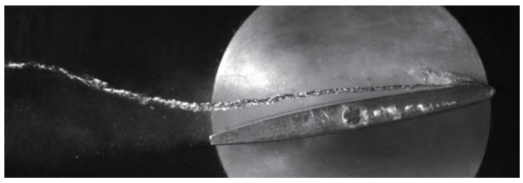

(a) experiment results from Dreyer et al. (2014)

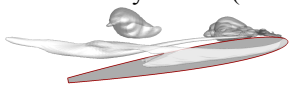

(b) cavitation region marked by the isosurface of vapor valume fraction $\alpha = 0.5$

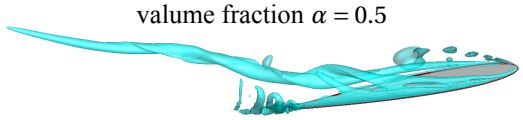

(c) isosurface of $Q = 1 \times 10^6$, full wet flow,

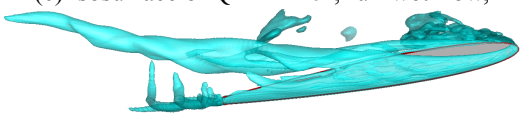

(d) isosurface of $Q = 1 \times 10^6$, cavitating flow

Figure 6: Comparisons on the vorticity region and cavitation region, $\tau = 1.0$.

results well, this mean that in this gap cavitation have no significant influence on the vortex trajectory. This phenomenon can also be find in Figure 6, although at a glance, there exist a huge difference between the vortex structure show in Figure 6 (c) and Figure 6 (d), but the differ is just in the length not in the trajectory. But for gaps $\tau \leq 0.7$，take $\tau = 0.7$, 0.4 and 0.1 for example, significant differences can be find between the tip leakage vortex and cavitating tip leakage vortex in Figure 7-9. Also in full wet flow many secondary vortex can be fund in the wing tip region, but in cavitation flow no such kinds of structures can be found. In order to have a clear understanding of the difference between cavitating and full wet flow, a quantitative analysis will be presented in the next stage.

From the qualitative analysis above, we can get this conclusion: for all cases of $\tau \geq 1$, they share the same law between the cavitating tip vortex and full wetted tip vortex but for all cases of $\tau \leq 0.7$ they share another law, so for brevity, a quantitative analysis of vortex trajectory of $\tau = 2$ and $\tau = 0.7$ will be discussed in this stage. Comparisons on the trajectories are shown in Figure 10 and Figure 11, the position of vortex trajectories (vortex centres) are the points where Q-criterion reach the peak.

From Figure 10 we can see clearly that the tip leakage trajectory of both cavitating flow and non-cavitating flow match very well with the experimental results, this mean that when $\tau \geq 1$, cavitation have no significant influence on tip leakage vortex. From Figure 11 only the results of cavitating flow can match the experimental results. In contrast, there is an apparent difference on the trajectories downward the hydrofoil when the gap size is smaller than $\tau = 1.0$.

5 CONCLUSIONS

We perform the numerical simulations for the tip leakage vortex for both full wet and cavitating flows by solving the

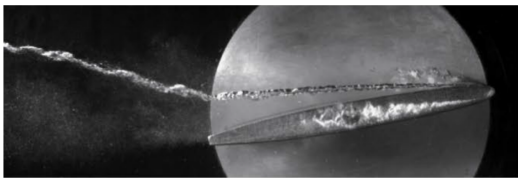

(a) experiment results from Dreyer et al. (2014)

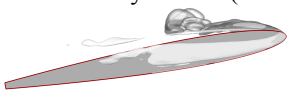

(b) cavitation region marked by the isosurface of vapor valume fraction $\alpha = 0.5$

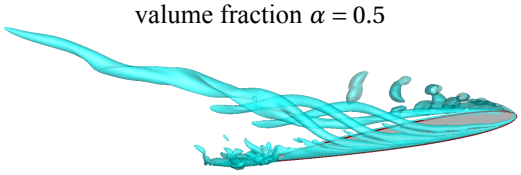

(c) isosurface of $Q = 1 \times 10^6$, full wet flow,

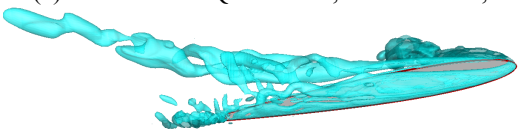

(d) isosurface of $Q = 1 \times 10^6$, cavitating flow

Figure 7: Comparisons on the vorticity region and cavitation region, $\tau = 0.7$.

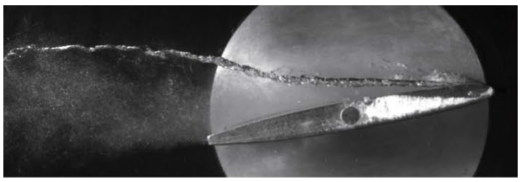

(a) experiment results from Dreyer et al. (2014)

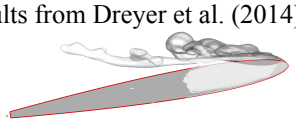

(b) cavitation region marked by the isosurface of vapor valume fraction $\alpha = 0.5$

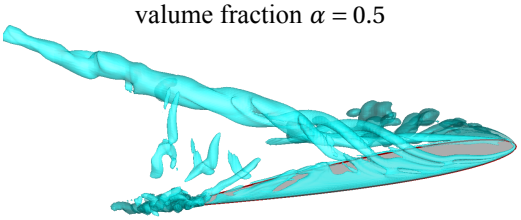

(c) isosurface of $Q = 1 \times 10^6$, full wet flow,

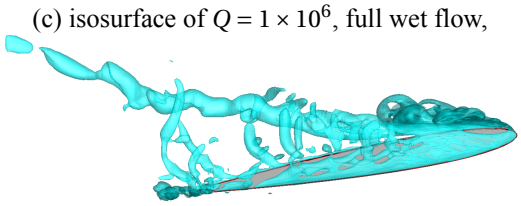

(d) isosurface of $Q = 1 \times 10^6$, cavitating flow

Figure 8: Comparisons on the vorticity region and cavitation region, $\tau = 0.4$.

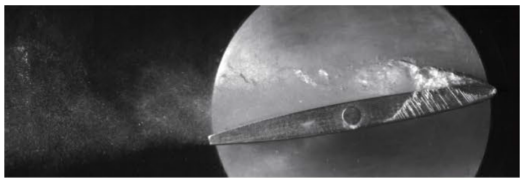

(a) experiment results from Dreyer et al. (2014)

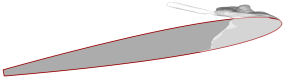

(b) cavitation region marked by the isosurface of vapor valume fraction $\alpha = 0.5$

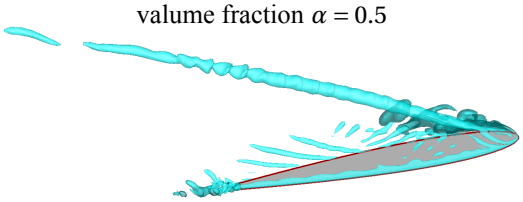

(c) isosurface of $Q = 1 \times 10^6$, full wet flow,

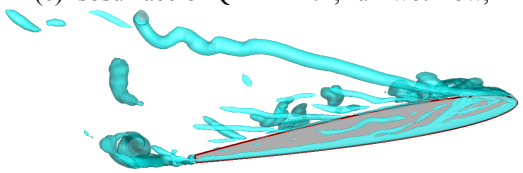

(d) isosurface of $Q = 1 \times 10^6$, cavitating flow

Figure 9: Comparisons on the vorticity region and cavitation region, $\tau = 0.1$.

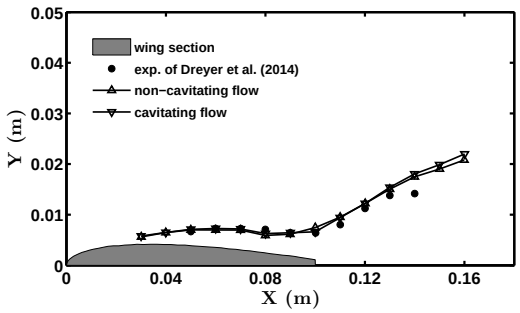

Figure 10: tip-leakage vortex trajectory of $\tau = 2$.

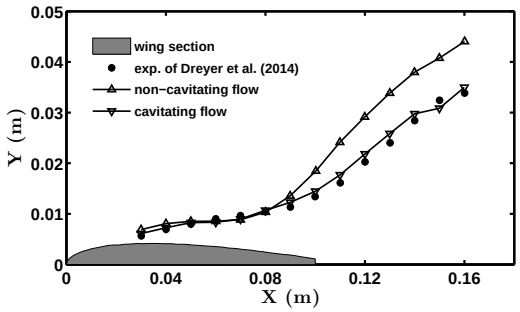

Figure 11: tip-leakage vortex trajectory of $\tau = 0.7$.

RANS equations with the nonlinear k-ε turbulence model. From the comparisons between the numerical results and experimental data, it is found that the proposed approach can capture the main characteristics of the tip leakage vortex flows at a moderate computational cost. By comparing the vortex trajectories between numerical and experimental results, we can get this conclusion: when $\tau \geq 1$, cavitation have no significant influence on tip leakage vortex, when $\tau \leq 0.7$, an apparent difference on the vortex trajectories can be see between the full wet and cavitating flows, it means that with condition of $\tau \leq 0.7$, cavitation have a significant influence on tip leakage vortex.

REFERENCES

Chow, J. S., Zilliac, G. G. and Bradshaw, P. (1997). 'Mean and Turbulence Measurements in the Near Field of a Wingtip Vortex'. AIAA Journal **35**(10), 1561--1567.

Churchfield, M. J. and Blaisdell, G. A. (2009). 'Numerical Simulations of a Wingtip Vortex in the Near Field'. Journal of Aircraft **46**(1), 230--243.

Decaix, J., Balarac, G., Dreyer, M., Farhat, M. and Münch, C. (2015). 'RANS and LES computations of the tip-leakage vortex for different gap widths'. Journal of Turbulence **16**(4), 309--341.

Dreyer, M., Decaix, J., Münch-Alligné, C. and Farhat, M. (2014). 'Mind the gap: a new insight into the tip leakage vortex using stereo-PIV'. Experiments in Fluids **55**(11), 1849.

Giuni, M. (2013). Formation and early development of wingtip vortices. PhD thesis. University of Glasgow.

Jeong, J. and Hussain, F. (1995). 'On the identification of a vortex'. Journal of Fluid Mechanics **285**, 69--94.

Launder, B. E. and Spalding, D. B. (1974). 'The numerical computation of turbulent flows'. Computer methods in applied mechanics and engineering **3**(2), 269--289.

Salvatore, F., Streckwall, H. and van Terwisga, T. (2009). 'Propeller cavitation modelling by CFD—results from the VIRTUE 2008 rome workshop'. First International Symposium on Marine Propulsors SMP'09. Trondheim, Norway.

Schnerr, G. H. and Sauer, J. (2001). 'Physical and Numerical Modeling of Unsteady Cavitation Dynamics'. ICMF-2001, 4th International Conference on Multiphase Flow. New Orleans, USA.

Singhal, A. K., Athavale, M. M., Li, H. and Jiang, Y. (2002). 'Mathematical Basis and Validation of the Full Cavitation'. Journal of fluids engineering **124**(3), 617--624.

Sipilä, T., Siikonen, T. and Saisto, I. (2011). 'FINFLO RANS-Predictions for Propeller Performance'. Second International Symposium on Marine Propulsors SMP'11. Hamburg, Germany.

Vaz G, Hally D, Huuva T, et al (2015). 'Cavitating Flow Calculations for the E779A Propeller in Open Water and Behind Conditions: Code Comparison and Solution Validation'. Fourth International Symposium on Marine Propulsors SMP'15. Austin, Texas, USA.

You, D., Wang, M., Moin, P. and Mittal, R. (2007). 'Large-eddy simulation analysis of mechanisms for viscous losses in a turbomachinery tip-clearance flow'. Journal of Fluid Mechanics **586**, 177--204.

Zhu, J. and Shih, T. H. (1994). 'Computation of confined coflow jets with three turbulence models'. International journal for numerical methods in fluids **19**(10), 939--956.

Zwart, P. J., Gerber, A. G. and Belamri, T. (2004). 'A two-phase flow model for predicting cavitation dynamics'. Fifth International Conference on Multiphase Flow. Yokohama, Japan.

DISCUSSION

Question from Xiaoxing Peng

Can you explain the differences between standard k-ε model and nonlinear k-ε model?

Author's closure

The standard k-ε model is a linear turbulence model witch based on turbulent-viscosity hypothesis, but the nonlinear k-ε model is based on a nonlinear turbulent-viscosity models. In fact the nonlinear turbulent-viscosity models is reduced from algebraic stress model (ASM), so the nonlinear k-ε model used In this article is a simplified algebraic stress model.